Lecture Notes in Applied and Computational Mechanics 86

Jurica Sorić
Peter Wriggers
Olivier Allix *Editors*

Multiscale Modeling of Heterogeneous Structures

Springer

Lecture Notes in Applied and Computational Mechanics

Volume 86

This series aims to report new developments in applied and computational mechanics—quickly, informally and at a high level. This includes the fields of fluid, solid and structural mechanics, dynamics and control, and related disciplines. The applied methods can be of analytical, numerical and computational nature.

More information about this series at http://www.springer.com/series/4623

Jurica Sorić · Peter Wriggers
Olivier Allix
Editors

Multiscale Modeling of Heterogeneous Structures

Springer

Editors
Jurica Sorić
University of Zagreb
Zagreb
Croatia

Olivier Allix
LMT Cachan
Cachan
France

Peter Wriggers
Institute of Continuum Mechanics
Leibniz Universität Hannover
Hannover
Germany

ISSN 1613-7736 ISSN 1860-0816 (electronic)
Lecture Notes in Applied and Computational Mechanics
ISBN 978-3-319-65462-1 ISBN 978-3-319-65463-8 (eBook)
https://doi.org/10.1007/978-3-319-65463-8

Library of Congress Control Number: 2017949492

Printed on acid-free paper

This Springer imprint is published by Springer Nature
The registered company is Springer International Publishing AG
The registered company address is: Gewerbestrasse 11, 6330 Cham, Switzerland

Preface

Many engineering materials have a heterogeneous structure, especially at the microscopic scale. These are often referred to as multiphase materials, composite or heterogeneous materials. From an engineering point of view, multiphase materials are desirable because they can be tailor-made to take advantage of particular properties of each constituent. The size, shape, spatial distribution, volume fraction, and properties of the constituents at microstructural level have a significant impact on the behavior of material properties observed at the macroscale. Additionally, the external loading applied at macroscale might cause changes in the microstructural morphology, e.g., void formation, damage as well as cracking, which can put structural integrity at risk. In order to assess structural integrity and to predict structural lifetime, an analysis of the evolving microstructure is necessary. An efficient computational strategy enabling more realistic material description as well as deformation response is still a challenge in computational mechanics. Various multiscale techniques have been developed that model materials at multiple levels. Moreover, various modern experimental techniques provide access to a detailed characterization of the internal structure and processes taking place in materials at small scales, paving the way to new routes for model validation.

This book contains 18 papers that resulted from selected presentations at the workshop "Multiscale Modeling of Heterogeneous Structures" held September 21–23, 2016 in Dubrovnik, Croatia. The workshop focused on multiscale approaches and homogenization procedures as well as damage evaluation and crack initiation. Recent advances in the analysis and discretization of heterogeneous materials were addressed. The state of the art in this research area was highlighted with respect to different computational methods, software development, and applications to engineering structures.

The papers were allotted to four topics: Composites, Computational Solution Approaches, Gradient Enhanced Modeling, and Multiphysics and associated experimental techniques. The topic Composites covers defects in composite materials including their numerical and experimental investigations. Elastic as well as elastoplastic constitutive models are considered, where the modeling has been performed at macro- and microlevels. The second group of the papers is more

focused on novel computational schemes applied at the different scales. The validation of numerical results has been discussed. The quasi-brittle and the ductile damage using the gradient enhanced approach are considered in the frame of the topic Gradient Enhanced Modeling. Finally, the thermoplasticity, the solid-liquid mixture as well as the ferroelectric models are discussed in the fourth topic.

The workshop was held under the auspices of the German Association for Computational Mechanics (GACM), the Central European Association for Computational Mechanics (CEACM), the ENS Cachan, the Leibniz Universität Hannover, the Faculty of Mechanical Engineering, and Naval Architecture of the University of Zagreb. It was supported by the Alexander von Humboldt Foundation, the Deutsch-Französische Hochschule, and the Deutsche Forschungsgemeinschaft. The editors express their deep gratitude to all sponsoring institutions. Furthermore, the editors would like to thank Ms. Schulte and Dr. Lesičar for their engagement in the organization of the workshop as well as Dr. Weißenfels for his valuable assistance in preparing the book.

Zagreb, Croatia — Jurica Sorić
Hannover, Germany — Peter Wriggers
Cachan, France — Olivier Allix

Contents

Part I
Composites

Evolution of Failure Mechanisms in Composite Shell Structures Using Different Models

Werner Wagner and Friedrich Gruttmann

Abstract Modelling of structures on different scales has been a popular subject in the past. Within such a strategy the structural behaviour is modeled on a macro-level, describing the structure itself, whereas the material behaviour is modeled on a micro-level. Here typically RVEs are used. The proper choice of boundary conditions for the RVE is a difficult task in case of shell structures. Here, results have been presented for homogeneous and layered structures for composite materials in (Gruttmann & Wagner, Int J Num Meth Eng 94:1233–1254, 2013) [10]. In the present paper we discuss the influence of material nonlinear behaviour, especially the damage behaviour of fiber reinforced polymers, within the above described setting in comparison to other modeling techniques.

1 Introduction

Finite shell elements which are based on the first–order shear deformation theory are in general able to describe the global deformation behaviour of thin plate and shell structures. In [20] we presented results that show remarkable robustness of mixed formulations in nonlinear applications. Modifications of such mixed formulations to layered structures are developed in [9]. With respect to damage behaviour a layer-wise numerical integration has to be used. A similar approach can be achieved in case of solid shell elements, e.g. [14, 15]. Choosing one element in thickness direction

W. Wagner (✉)
Institut für Baustatik, Karlsruher Institut für Technologie,
Kaiserstr. 12, 76131 Karlsruhe, Germany
e-mail: w.wagner@kit.edu

F. Gruttmann
Fachgebiet Festkörpermechanik, Technische Universität Darmstadt,
Franziska-Braun-Str. 7, 64287 Darmstadt, Germany
e-mail: gruttmann@mechanik.tu-darmstadt.de

J. Sorić et al. (eds.), *Multiscale Modeling of Heterogeneous Structures*,
Lecture Notes in Applied and Computational Mechanics 86,
https://doi.org/10.1007/978-3-319-65463-8_1

again a layerwise approach has to be added. However for some stress components only an average shape through the thickness can be obtained. Various methods have been developed to obtain the complicated local stress state in inhomogeneous thin structures. So-called multi-director shell formulations with an appropriate number of global degrees of freedom at the nodes yield approximate solutions of the three-dimensional boundary value problem, e.g. [8, 18]. The application of brick elements or solid shell elements provides likewise a computationally expensive approach, e.g. [14, 15], but allow the description of warping or other effects in the cross section of the shell. For laminates each layer must be discretised with several elements in thickness direction to obtain satisfactory results. The enhancement of the displacement field by layer-wise linear (zig-zag) functions through the thickness, see e.g. [1], could be another option, which leads to a more precise deformation behaviour. New actual promising results for locally extended shell formulations can be found in [11] for the elastic case. A further alternative is the treatment of shells as a homogeneous continuum in a 2D shell environment with effective properties obtained through a homogenisation procedure to avoid large-scale computations. A large number of papers exists on computational homogenisation methods for general heterogeneous materials, see e.g. [5, 23] for a survey and new developments. Based on the formulation in [20] we have derived a two-scale model with a variational formulation and an associated linearisation for the coupled global–local boundary value problem in [10] and an adaptive application to local elasto-plastic material in [22]. In this paper we present the applicability to damaged composite shell structures. For that we compare different discretisation models

- layered solid shell models [14, 15]
- layerwise solid shell models [14, 15]
- layerwise shell models [9, 20]
- shell models with an internal FE^2-approach [2, 6, 10].

To do this we describe in the next two sections briefly the main equations of a two-scale shell model and the main equations of damage models of Hashin, e.g. [7, 12], Puck, e.g. [16] and Cuntze, e.g. [3, 4].

2 Two-Scale Shell Model

2.1 Theoretical Background

At first the basic equations of a Reissner-Mindlin shell model are summarised. Based on a reference surface the thickness coordinate $\xi^3 = z$ is defined, where h^- and h^+ are the z-coordinates of the outer surfaces. The shell is loaded statically by loads $\bar{\mathbf{p}}$ in Ω and by boundary forces $\bar{\mathbf{t}}$ on Γ_σ. The displacement field of the Reissner-Mindlin theory is obtained with

$$\bar{\mathbf{u}} = \bar{\mathbf{u}}_0 + z\,(\bar{\mathbf{d}} - \bar{\mathbf{D}}) \quad \bar{\mathbf{u}}_0 = \mathbf{x} - \mathbf{X}\,, \tag{1}$$

where $\mathbf{x}, \mathbf{X}$ denote the position vectors of the initial and current reference surface, respectively. The unit director vectors are denoted by $\bar{\mathbf{D}}, \bar{\mathbf{d}}$, where $\bar{\mathbf{d}}$ is a function of the rotational parameters $\bar{\omega}$.

The shell strains are derived from the Green-Lagrangian strain tensor using kinematic assumption (1) and are arranged in a vector as

$$\varepsilon(\bar{\mathbf{u}}_0, \bar{\omega}) = [\varepsilon_{11}, \varepsilon_{22}, 2\,\varepsilon_{12}, \kappa_{11}, \kappa_{22}, 2\,\kappa_{12}, \gamma_1, \gamma_2]^T\,. \tag{2}$$

Furthermore the vector of stress resultants σ with membrane forces $n^{\alpha\beta}$, bending moments $m^{\alpha\beta}$ and shear forces q^{α} is introduced via

$$\sigma = [n^{11}, n^{22}, n^{12}, m^{11}, m^{22}, m^{12}, q^1, q^2]^T\,. \tag{3}$$

Further details on the remarkable robust mixed formulation are described in [20] and [9]. According to Fig. 1 a representative volume element (RVE) at an integration point i of a particular finite shell element is introduced. The domain $\mathscr{B}_i$ extends through the total thickness h of the shell and has the size $l_x \times l_y \times h$. The displacement field is split in an averaged part $\bar{\mathbf{u}}$ and a fluctuation part $\tilde{\mathbf{u}}$.

$$\mathbf{u} = \bar{\mathbf{u}} + \tilde{\mathbf{u}}\,. \tag{4}$$

The averaged displacements $\bar{\mathbf{u}}$ according to (1) exhibit a linear shape of the thickness coordinate, whereas $\tilde{\mathbf{u}}$ describes warping and thickness change. The weak form of equilibrium of the coupled problem can now be written with $\mathbf{v} = [\bar{\mathbf{u}}_0, \bar{\omega}, \mathbf{u}]^T$ and associated admissible variations

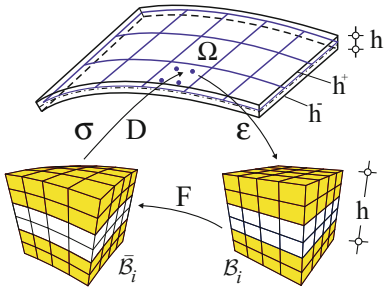

Fig. 1 Computational homogenisation of a layered shell

$$g(\mathbf{v},\delta\mathbf{v}) = \int_{\Omega_1} (\sigma\cdot\delta\varepsilon - \bar{\mathbf{p}}\cdot\delta\bar{\mathbf{u}}_0)\,dA_1 + \int_{\Omega_2} (\sigma\cdot\delta\varepsilon - \bar{\mathbf{p}}\cdot\delta\bar{\mathbf{u}}_0)\,dA_2 + \sum_{e=1}^{ne2}\sum_{i=1}^{NGP}\frac{1}{A_i}\int_{\Omega_i}\int_{h^-}^{h^+}\mathbf{S}\cdot\delta\mathbf{E}\;\bar{\mu}\;dz\;dA - \int_{\Gamma_\sigma}\bar{\mathbf{t}}\cdot\delta\bar{\mathbf{u}}_0\,ds = 0\,. \tag{5}$$

The structure is divided in parts Ω_1 without and Ω_2 with a two-scale model, respectively. Furthermore $ne1$ and $ne2$ denote the associated number of shell elements within a discretisation. NGP is the number of Gauss points for each element and $A_i = l_x\,l_y$ is the reference area of the RVE. On the RVE $\mathbf{S}$ denotes the Second Piola-Kirchhoff stress tensor with $\mathbf{P} = \mathbf{F}\,\mathbf{S}$ and the virtual Green-Lagrangian strain tensor is introduced via $\delta\mathbf{E} = \frac{1}{2}(\delta\mathbf{F}^T\mathbf{F} + \mathbf{F}^T\delta\mathbf{F})$. For the finite element formulation of the next section we need to derive the linearisation of Eq. (5). With conservative loads $\bar{\mathbf{p}}$ and $\bar{\mathbf{t}}$ one obtains

$$L\,[g(\mathbf{v},\delta\mathbf{v}),\,\Delta\mathbf{v}] := g(\mathbf{v},\delta\mathbf{v}) + Dg\cdot\Delta\mathbf{v} \tag{6}$$

where $g(\mathbf{v},\delta\mathbf{v})$ is given in (5) and

$$Dg\cdot\Delta\mathbf{v} = \int_{\Omega_1}(\Delta\sigma\cdot\delta\varepsilon + \sigma\cdot\Delta\delta\varepsilon)\,dA_1 + \int_{\Omega_2}(\Delta\sigma\cdot\delta\varepsilon + \sigma\cdot\Delta\delta\varepsilon)\,dA_2 + \sum_{e=1}^{ne2}\sum_{i=1}^{NGP}\frac{1}{A_i}\int_{\Omega_i}\int_{h^-}^{h^+}(\Delta\mathbf{S}:\delta\mathbf{E} + \mathbf{S}:\Delta\delta\mathbf{E})\;dz\;dA \tag{7}$$

with $\Delta\sigma = \mathbf{D}\Delta\varepsilon$, $\Delta\mathbf{S} = \mathbf{C}\Delta\mathbf{E}$ and $\Delta\delta\mathbf{E} = \frac{1}{2}(\delta\mathbf{F}^T\Delta\mathbf{F} + \Delta\mathbf{F}^T\delta\mathbf{F})$. The material matrix $\mathbf{C}$ is a standard output of a library of constitutive laws in a material description. The linearised virtual shell strains $\Delta\delta\varepsilon$ are derived for finite rotations in [20]. The stress resultant vector σ and the matrix of linearised stress resultants $\mathbf{D}$ are specified within the finite element formulation in the next section.

2.2 Finite Element Formulation

The reference surface of the shell is discretised with $ne = ne1 + ne2$ quadrilateral isoparametric shell elements, using bilinear shape functions $N_I(\xi,\eta)$ which are arranged in the matrix $\mathbf{N}$. The nodal degrees of freedom are three displacements and two or three rotations. Inserting these interpolation functions into the linearised weak form (6) considering (5) and (7) yields

$$L\left[g(\mathbf{v}^h, \delta\mathbf{v}^h), \Delta\mathbf{v}^h\right] = \sum_{e=1}^{ne1} \delta\mathbf{v}_e^G \mathbf{k}_e^G \Delta\mathbf{v}_e^G + \mathbf{f}_e^G + \sum_{e=1}^{ne2}$$

$$\begin{bmatrix} \delta\mathbf{v}^G \\ \delta\mathbf{V}_1 \\ \vdots \\ \delta\mathbf{V}_i \\ \vdots \\ \delta\mathbf{V}_{NGP} \end{bmatrix}_e^T \left\{ \begin{bmatrix} \mathbf{k}^G & \mathbf{0} & \vdots & \mathbf{0} & \vdots & \mathbf{0} \\ \mathbf{0} & \mathbf{K}_1^L & \vdots & \mathbf{0} & \vdots & \mathbf{0} \\ \dots & \dots & \ddots & \mathbf{0} & \dots & \dots \\ \mathbf{0} & \mathbf{0} & \mathbf{0} & \mathbf{K}_i^L & \mathbf{0} & \mathbf{0} \\ \dots & \dots & \dots & \mathbf{0} & \ddots & \dots \\ \mathbf{0} & \mathbf{0} & \dots & \mathbf{0} & \dots & \mathbf{K}_{NGP}^L \end{bmatrix}_e \begin{bmatrix} \Delta\mathbf{v}^G \\ \Delta\mathbf{V}_1 \\ \vdots \\ \Delta\mathbf{V}_i \\ \vdots \\ \Delta\mathbf{V}_{NGP} \end{bmatrix}_e + \begin{bmatrix} \mathbf{f}^G(\sigma_i) \\ \mathbf{F}_1^L \\ \vdots \\ \mathbf{F}_i^L \\ \vdots \\ \mathbf{F}_{NGP}^L \end{bmatrix}_e \right\} \tag{8}$$

The indices G and L refer to the global and local boundary value problems, respectively. The matrices of the first row in (8) follow from the global part of the linearised weak form. The element residual vector and the tangential element stiffness matrix read

$$\begin{aligned} \mathbf{f}^G(\sigma_i) &= \int_{\Omega_e} (\mathbf{B}^T\sigma - \mathbf{N}^T\bar{\mathbf{p}})\, dA - \int_{\Gamma_{\sigma e}} \mathbf{N}^T\bar{\mathbf{t}}\, ds \mathbf{k}^G(\mathbf{D}_i) \\ &= \int_{\Omega_e} (\mathbf{B}^T\mathbf{D}\,\mathbf{B} + \mathbf{G})\, dA \end{aligned} \tag{9}$$

where the matrices $\mathbf{B}$ and $\mathbf{G}$ are derived in [20]. The vector of stress resultants σ_i and linearised stress resultants $\mathbf{D}_i$ are specified below. The matrices of the second to the last row in (8) are associated with the local boundary value problems at Gauss points $1 \le i \le NGP$ of shell element e and occur only, if a two-scale model is used. A local boundary value problem can be defined at Gauss point i

$$\delta\mathbf{V}_i^T (\mathbf{K}_i^L \Delta\mathbf{V}_i + \mathbf{F}_i^L) = \frac{1}{A_i} \sum_{e=1}^{Ne} \delta\mathbf{v}_e^T (\mathbf{k}_e^L \Delta\mathbf{v}_e + \mathbf{f}_e^L)\,. \tag{10}$$

Here, the total number of elements used for the discretisation of the RVE is denoted by Ne. The element residual vector $\mathbf{f}_e^L$ and the tangential element stiffness matrix $\mathbf{k}_e^L$ read

$$\mathbf{f}_e^L = \int_{(V_e)} \tilde{\mathbf{B}}^T \mathbf{S}\, dV \qquad \mathbf{k}_e^L = \int_{(V_e)} (\tilde{\mathbf{B}}^T \mathbf{C}\, \tilde{\mathbf{B}} + \tilde{\mathbf{G}})\, dV \tag{11}$$

where $\tilde{\mathbf{B}}$ and $\tilde{\mathbf{G}}$ are the virtual strain displacement matrix and the geometrical matrix of 8-noded solid shell elements, respectively. The element displacement vector $\mathbf{v}_e$ is now split in a part $\mathbf{v}_\Omega$ with internal displacements and a part $\mathbf{v}_\Gamma$ which contains displacements on the boundary Γ_u of the RVE

$$\mathbf{v}_e = \begin{bmatrix} \mathbf{v}_\Omega \\ \mathbf{v}_\Gamma \end{bmatrix} = \begin{bmatrix} \mathbf{a}_e\, \mathbf{V}_i \\ \mathbf{A}_e\, \varepsilon_i \end{bmatrix}. \tag{12}$$

In Eq. (12) $\mathbf{a}_e$ is a standard assembly matrix. $\mathbf{A}_e$ is defined for *nel* nodes on the element with

$$\mathbf{A}_e = [\delta_1 \mathbf{A}_1, \dots, \delta_I \mathbf{A}_I, \dots, \delta_{nel} \mathbf{A}_{nel}]^T \tag{13}$$

with $\delta_I = 0$ for internal nodes and $\delta_I = 1$ for boundary nodes. Assuming small strains the relation of the boundary displacements to the shell strains ε can be written as

$$\begin{bmatrix} v_x \\ v_y \end{bmatrix}_I = \mathbf{A}_I(x,y,z)\,\varepsilon_i = \begin{bmatrix} x & 0 & \frac{1}{2}y & xz & 0 & \frac{1}{2}yz & z & 0 \\ 0 & y & \frac{1}{2}x & 0 & yz & \frac{1}{2}xz & 0 & z \end{bmatrix}_I \begin{bmatrix} \varepsilon_{11} \\ \varepsilon_{22} \\ 2\varepsilon_{12} \\ \kappa_{11} \\ \kappa_{22} \\ 2\kappa_{12} \\ \gamma_1 \\ \gamma_2 \end{bmatrix}_i \tag{14}$$

Based on the element displacement split (12) one can introduce submatrices of $\mathbf{k}_e^L$ and $\mathbf{f}_e^L$ in (10)

$$\begin{aligned} &\delta\mathbf{V}_i^T\,(\mathbf{K}_i^L\,\Delta\mathbf{V}_i + \mathbf{F}_i^L) \\ &= \frac{1}{A_i}\sum_{e=1}^{Ne} \begin{bmatrix} \delta\mathbf{V}_i \\ \delta\varepsilon_i \end{bmatrix}^T \left\{ \begin{bmatrix} \mathbf{a}_e^T\,\mathbf{k}_{\Omega\Omega}\,\mathbf{a}_e & \mathbf{a}_e^T\,\mathbf{k}_{\Omega\Gamma}\,\mathbf{A}_e \\ \mathbf{A}_e^T\,\mathbf{k}_{\Gamma\Omega}\,\mathbf{a}_e & \mathbf{A}_e^T\,\mathbf{k}_{\Gamma\Gamma}\,\mathbf{A}_e \end{bmatrix}_e \begin{bmatrix} \Delta\mathbf{V}_i \\ \Delta\varepsilon_i \end{bmatrix} + \begin{bmatrix} \mathbf{a}_e^T\,\mathbf{f}_\Omega \\ \mathbf{A}_e^T\,\mathbf{f}_\Gamma \end{bmatrix}_e \right\} \\ &= \frac{1}{A_i} \begin{bmatrix} \delta\mathbf{V}_i \\ \delta\varepsilon_i \end{bmatrix}^T \left\{ \begin{bmatrix} \mathbf{K} & \mathbf{L} \\ \mathbf{L}^T & \mathbf{M} \end{bmatrix} \begin{bmatrix} \Delta\mathbf{V}_i \\ \Delta\varepsilon_i \end{bmatrix} + \begin{bmatrix} \mathbf{F}_\Omega \\ \mathbf{F}_\Gamma \end{bmatrix} \right\}. \end{aligned} \tag{15}$$

The internal degrees of freedom $\Delta\mathbf{V}_i$ can now be eliminated from the set of equations which yields the final form of Eq. (15)

$$\delta\mathbf{V}_i^T\,(\mathbf{K}_i^L\,\Delta\mathbf{V}_i + \mathbf{F}_i^L) = \delta\varepsilon_i^T(\mathbf{D}_i\,\Delta\varepsilon_i + \sigma_i) \tag{16}$$

where the stress resultants and linearised stress resultants of Gauss point i are defined using $\mathbf{KX} = \mathbf{L}$ and $\mathbf{KY} = \mathbf{F}_\Omega$

$$\sigma_i = \frac{1}{A_i}(\mathbf{F}_\Gamma - \mathbf{L}^T\mathbf{Y}) \quad \mathbf{D}_i = \frac{1}{A_i}(\mathbf{M} - \mathbf{L}^T\mathbf{X})\,. \tag{17}$$

Finally (16) is inserted into the linearised coupled global-local boundary value problem (8)

$$L\left[g(\mathbf{v}^h, \delta\mathbf{v}^h), \Delta\mathbf{v}^h\right] = \sum_{e=1}^{ne1} \delta\mathbf{v}_e^G \mathbf{k}_e^G \Delta\mathbf{v}_e^G + \mathbf{f}_e^G + \sum_{e=1}^{ne2}$$

$$\begin{bmatrix} \delta\mathbf{v}^G \\ \delta\varepsilon_1 \\ \vdots \\ \delta\varepsilon_i \\ \vdots \\ \delta\varepsilon_{NGP} \end{bmatrix}_e^T \left\{ \begin{bmatrix} \mathbf{k}^G(\mathbf{D}_i) & \mathbf{0} & \vdots & \mathbf{0} & \vdots & \mathbf{0} \\ \mathbf{0} & \mathbf{D}_1 & \vdots & \mathbf{0} & \vdots & \mathbf{0} \\ \cdots & \cdots & \ddots & \mathbf{0} & \cdots & \cdots \\ \mathbf{0} & \mathbf{0} & \mathbf{0} & \mathbf{D}_i & \mathbf{0} & \mathbf{0} \\ \cdots & \cdots & \cdots & \mathbf{0} & \ddots & \cdots \\ \mathbf{0} & \mathbf{0} & \cdots & \mathbf{0} & \cdots & \mathbf{D}_{NGP} \end{bmatrix}_e \begin{bmatrix} \Delta\mathbf{v}^G \\ \Delta\varepsilon_1 \\ \vdots \\ \Delta\varepsilon_i \\ \vdots \\ \Delta\varepsilon_{NGP} \end{bmatrix}_e + \begin{bmatrix} \mathbf{f}^G(\sigma_i) \\ \sigma_1 \\ \vdots \\ \sigma_i \\ \vdots \\ \sigma_{NGP} \end{bmatrix}_e \right\} \tag{18}$$

It has been shown, see e.g. [21], that the equivalence of macroscopic and microscopic stress power for shell structures, the so called Hill condition, holds

$$\frac{1}{h}\sigma\dot{\epsilon} = \frac{1}{V}\int_V \mathbf{S} : \dot{\mathbf{E}}\, dV = \frac{1}{V}\int_A \mathbf{t}\cdot\dot{\tilde{\mathbf{u}}}\, dA \quad \text{with} \quad \dot{\tilde{\mathbf{u}}}_I = \begin{bmatrix} \dot{\tilde{u}}_x \\ \dot{\tilde{u}}_y \end{bmatrix}_I = \mathbf{A}_I\,\dot{\epsilon} \tag{19}$$

3 Failure Models of Hashin, Puck and Cuntze

For fiber reinforced composite structures a range of failure mechanisms as fiber fracture (FF), inter fiber failure (IFF) and delamination may occur. Several failure models are proposed to describe FF (Fig. 2a, b) and IFF, usually each distinct in a tensile(t) and compressive(c) mode, (Fig. 2c, d). Improved models subdivide the IFF compressive mode in a shear dominant (Fig. 2d) and purely compression dominant mode (Fig. 2e). FF is the most severe failure and generally leads to structural collapse.

Based on a large number of models we choose the modified Hashin-model [7] as one of the most commercial ones. Furthermore we employ the Puck-model [16] and the Cuntze-model [3], which provide approaches to the physical aspects of the fracture. We describe the main equations. For a further discussion we refer to the original references.

3.1 The Modified Hashin-Model

One of the used failure models is the modified Hashin-model [7], based on the original version in [12]. The model consists of five failure criteria where the equations separate tensile and compressive matrix(M)- and fiber(F)-failure (M^t is used if $S_{22} > 0$, M^c if $S_{22} < 0$).

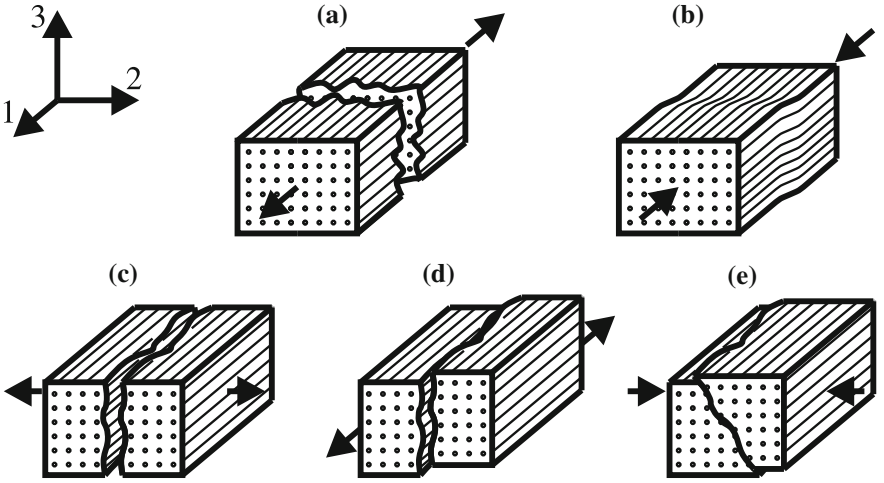

Fig. 2 Possible failure modes of a single ply of composite laminates: **a** tensile FF **b** compressive FF **c** tensile IFF **d** shear-dominant IFF **e** compressive IFF

$$
\begin{aligned}
\mathrm{F}^t: &\quad \left(\frac{S_{11}}{R_{\parallel}^t}\right)^2 = 1, \quad S_{11} > 0 \\
\mathrm{F}^c: &\quad \left(\frac{S_{11}}{R_{\parallel}^c}\right)^2 = 1, \quad S_{11} < 0 \\
\mathrm{M}^t: &\quad \left(\frac{S_{22}}{R_{\perp}^t}\right)^2 + \left(\frac{S_{12}}{R_{\perp\parallel}}\right)^2 + \left(\frac{S_{13}}{R_{\perp\parallel}}\right)^2 + \left(\frac{S_{23}}{R_{\perp\perp}}\right)^2 = 1 \\
\mathrm{M}^c: &\quad \left(\frac{S_{22}}{2R_{\perp\perp}}\right)^2 + \left[\left(\frac{R_{\perp}^c}{2R_{\perp\perp}}\right)^2 - 1\right]\frac{S_{22}}{R_{\perp}^c} + \left(\frac{S_{12}}{R_{\perp\parallel}}\right)^2 + \left(\frac{S_{13}}{R_{\perp\parallel}}\right)^2 + \left(\frac{S_{23}}{R_{\perp\perp}}\right)^2 = 1 \\
\mathrm{FMS}: &\left(\frac{\langle -S_{11}\rangle}{R_{\parallel}^c}\right)^2 + \left(\frac{S_{12}}{R_{\perp\parallel}}\right)^2 + \left(\frac{S_{13}}{R_{\perp\parallel}}\right)^2 = 1
\end{aligned}
\tag{20}
$$

The most important modification is the fiber-matrix-shear (FMS)-condition. This cut-off considers the shear load additional via

$$
\langle -S_{11}\rangle = \begin{cases} 0, & S_{11} \geq 0 \\ S_{11}, & S_{11} < 0 \end{cases} . \tag{21}
$$

The failure model is used ply-by-ply, thus every single layer is treated exclusively. S_{ij} are stresses referring to a local coordinate system, where the 1-direction specifies the fiber-direction, the 2-direction the in-plane direction normal to the fibers and the 3-direction is the through-thickness direction. Associated material strength values are

defined typically with $R^t_{\parallel}$, $R^c_{\parallel}$, $R^t_{\perp}$, $R^c_{\perp}$, $R_{\perp\parallel}$, $R_{\perp\perp}$ where subscripts $\parallel$ and $\perp$ denote the directions parallel and transverse to the fiber direction.

3.2 The Puck-Model

The Puck-model is used as a second model to predict failure of composite laminates. All equations and contents of this subsection refer to [16]. To describe the individual failure mode Puck introduces four different failure conditions. Each layer can fail in different modes, a FF and three IFF-conditions with tensile (IFFA), compressive (IFFC) and shear dominant inter fiber failure (IFFB).

$$
\begin{aligned}
&\text{FF:} \quad \varepsilon_{FF} = \left(\frac{\langle S_{11}\rangle}{R^t_{\parallel}}\right)^2 + \left(\frac{\langle -S_{11}\rangle}{R^c_{\parallel}}\right)^2 = 1 \\
&\text{IFF A:} \; \varepsilon_{IFF\,A} = \sqrt{\left(\frac{S_{12}}{R_{\perp\parallel}}\right)^2 + \left(1 - p^t_{\perp\parallel}\frac{R^t_{\perp}}{R_{\perp\parallel}}\right)^2 \left(\frac{S_{22}}{R^t_{\perp}}\right)^2} + p^t_{\perp\parallel}\frac{S_{22}}{R_{\perp\parallel}} = 1, \quad S_{22} > 0 \\
&\text{IFF B:} \; \varepsilon_{IFF\,B} = \frac{1}{R_{\perp\parallel}}\left(\sqrt{S^2_{12} + \left(p^c_{\perp\parallel}S_{22}\right)^2} + p^c_{\perp\parallel}S_{22}\right) = 1 \\
&\text{IFF C:} \; \varepsilon_{IFF\,C} = \left[\left(\frac{S_{12}}{2\left(1 + p^c_{\perp\perp}\right)R_{\perp\parallel}}\right)^2 + \left(\frac{S_{22}}{R^c_{\perp}}\right)^2\right]\frac{R^c_{\perp}}{(-S_{22})} = 1
\end{aligned}
\tag{22}
$$

Equation (22) defines efforts $Eff_{(mode)}$. Failure occur for $Eff_i > 1$. Curve fitting parameters appear which can be used to fit the failure model to a single material or an experiment. For carbon fiber reinforced plastics Puck [17] proposes $p^t_{\perp\parallel} = 0.35$, $p^c_{\perp\parallel} = 0.30$, $p^t_{\perp\perp} = 0.25 - 0.30$, $p^c_{\perp\perp} = 0.25 - 0.30$.

3.3 The Cuntze-Model

As a third model for composite laminates the Cuntze failure model is used. All equations and contents of this subsection refer to [3, 4]. To describe an individual failure mode Cuntze [3] introduces five failure conditions. Each layer can fail in different modes, two FF and three IFF-conditions. The FF-conditions distinguish tensile (FF1) and compressive fiber failure (FF2), and the IFF-conditions can be divided into tensile (IFF1), compressive (IFF3) and shear dominant inter fiber failure (IFF2).

$$
\begin{aligned}
&\text{FF1:} \quad \frac{I_1}{R^t_{\parallel}} = 1 \\
&\text{FF2:} \quad \frac{-I_1}{R^c_{\parallel}} = 1 \\
&\text{IFF1:} \quad \frac{I_2 + \sqrt{I_4}}{R^t_{\perp}} = 1 \\
&\text{IFF2:} \quad \frac{\sqrt{I_3^3 + b_{\perp\parallel}(I_2 I_3 - I_5)}}{(R_{\perp\parallel})^3} = 1 \\
&\text{IFF3:} \quad \frac{(b^{\tau}_{\perp} - 1) I_2 + b^{\tau}_{\perp}\sqrt{I_4}}{R^t_{\perp}} = 1
\end{aligned}
\tag{23}
$$

with

$$
\begin{aligned}
I_1 &= S_{11} & I_2 &= S_{22} \\
I_3 &= S_{22}^2 + S_{13}^2 & I_4 &= S_{22}^2 + 4S_{23}^2 \\
I_5 &= S_{22}(S_{13}^2 - S_{12}^2) - 4S_{12}S_{13}S_{23}
\end{aligned}
\tag{24}
$$

In Eq. (24) two curve fitting parameters appear which can be used to fit the failure model to a single material or an experiment. For carbon fiber reinforced plastics Cuntze [4] propose $0.05 < b_{\perp\parallel} < 0.15$, and $1.0 < b^{\tau}_{\perp} < 1.15$). Equation (23) defines stress efforts $Eff_{(mode)}$ for each failure mode which depends only on one material strength. They can be combined to a more realistic numerical model via

$$
Eff^{\dot{m}}_{(res)} = \sum_{i=1}^{5} Eff^{\dot{m}}_{(i)}. \tag{25}
$$

Here, a third curve fitting parameter $\dot{m}$ ('rounding-off-parameter') is used, which considers an interaction of the failure modes. A value of $\dot{m} \approx 3.0$ is recommended, see [4].

4 Example-Four Point Bending Test

4.1 Problem Description

The developed algorithms and elements are implemented in an extended version of the general finite element program FEAP [19]. The investigated example is a four point bending test, depicted in Fig. 3. The geometrical data are L = 400 mm, B = 12.5 mm, D = 20 mm and a layer thickness of t = 2.5 mm together with a stacking sequence $[0°/90°]_{2s}$. With respect to symmetry only one half of the structure is

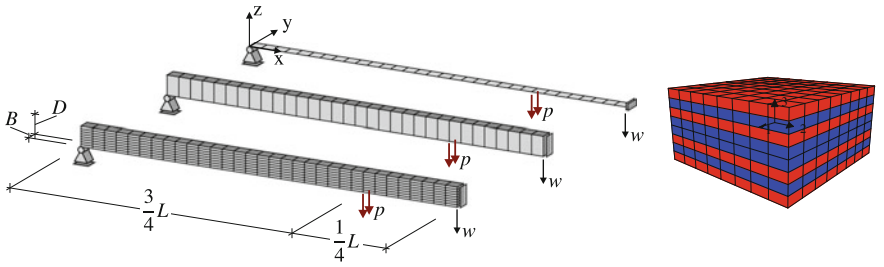

Fig. 3 Four point bending test: geometry, loading and discretisation options

discretised. A discretisation with solid shell elements [15] is chosen with 32×1 elements in x-y-plane. Furthermore the 1-Element-8-Layer model ('Solid Shell 1(8)') has one element in thickness direction and 8 layers, whereas the 8-Element-1-Layer model ('Solid Shell 8(1)') has for each layer one element in thickness direction. The discretisation with shell elements [20] is chosen with 32×1 elements in x-y-plane ('Shell (8)'). The thickness direction is modeled within a layerwise approach. With respect to the multi-scale approach the same shell model is used. Here, on RVE-level, discretisations using solid shell elements are applied. Again an option with 1-Element-8-Layer ($8 \times 8 \times 1(8)$ named 'Shell FE2 1(8)') and an option with 8-Element-1-Layer ($8 \times 8 \times 8(1)$ named 'Shell FE2 8(1)') in thickness direction could be used. The global boundary conditions are chosen as $u_z = 0$ at $x = 0$ and symmetry conditions at $x = L$. Furthermore plain strain conditions are assumed with $u_y = 0$ at $y = 0$ and $y = B$. It is well known, that in case of local stress based failure models a mesh dependency of solutions may occur. This is not topic of present paper. As stated above, we compare different discretisation options but introduce comparable meshes. The underlying material data for A-S Epoxy1 are depicted in Tables 1 and 2. Results are presented for the different shell and failure models in the following. The analysis is performed geometrically and material nonlinear on global as well as on local level. An arc-length scheme with displacement control is adopted. Load-deflection curves and damage distributions are depicted for the different cases. Different failure modes are shown with values between 0 (no damage) and 1 (fully

Table 1 A-S Epoxy1 stiffness values

$E_\parallel$ [MPa]	$E_\perp$ [MPa]	$\nu_{\parallel\perp}$ [-]	$G_{\parallel\perp}$ [MPa]	$G_{\perp\perp}$ [MPa]
140000	10000	0.3	6000	3335

Table 2 A-S Epoxy1 strength values

$R^t_\parallel$ [MPa]	$R^c_\parallel$ [MPa]	$R^t_\perp$ [MPa]	$R^c_\perp$ [MPa]	$R_{\perp\parallel}$ [MPa]
1990	1500	38	150	70

damaged) for solid shell and multi-scale models. The failure behaviour is plotted layerwise since no averaging in thickness direction is allowed.

The general deformation behaviour, see Fig. 5, is as follows. A nearly linear load-deflection behaviour occurs until a value of approximately w = 70 mm. The failure modes start with a matrix-failure in the 90°-layer at bottom in the loading region, when reaching $R^t_\perp$. The drastic reduction of the load is then based mainly on the fiber failure in the 0°-layer at top in the loading region, when reaching $R^c_\parallel$. Note $R^c_\parallel < R^t_\parallel$. Further loading leads to another matrix-failure in the 90°-layer at top in the loading region, with respect to $R^c_\perp$. Further minor mixed shear failure modes occur.

4.2 Hashin-Model

Figure 4 presents the deformed meshes at the final deformation of w = 100 mm for the different models. Figure 5 depicts load-deflection curves for different discretisation models for the case of the Hashin failure model. Depicted are results for the external load p [N/mm^2] with respect to the center deflection w [mm], see Fig. 3. Relatively similar results are produced for a discretisation 'Solid Shell 1(8) and a standard shell formulation 'Shell (8)'. Results for 'Solid Shell 1(8)' and 'Solid Shell 8(1)' differ in the post-failure region. 'Solid Shell 8(1)' and 'Shell (8)' lead to nearly similar results, even in the post-failure region. The multi-scale solutions 'Shell FE2 1(8)' and 'Shell FE2 8(1)' deviate from the 'Solid Shell 8(1)' solutions. A lower failure load and different post-failure paths are reached. This will be discussed in more detail in the following. Figure 6 presents the failure behaviour at w =100 mm in the solid model 'Solid Shell 8(1)', which is dominated by failures $M^c(0°)$ and $M^t(90°)$, $M^c(90°)$. A much more detailed analysis is possible for the multi-scale model, which is presented in Fig. 7. Here different failure modes are presented on the RVE, chosen here for

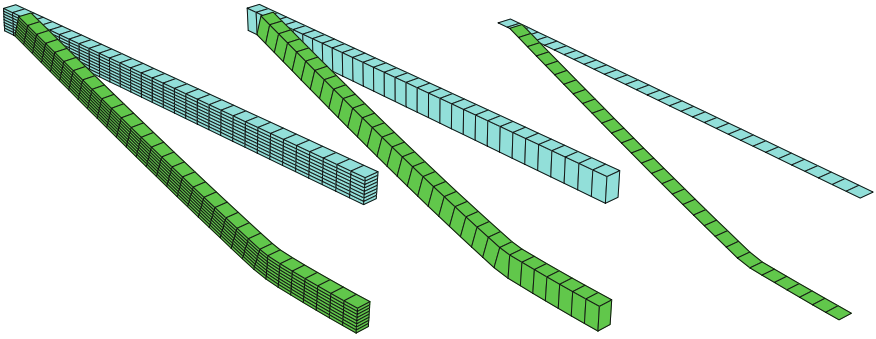

Fig. 4 Hashin. Deformed mesh Solid Shell 8(1), Solid Shell 1(8) versus Shell+FE2 at w = 100 mm

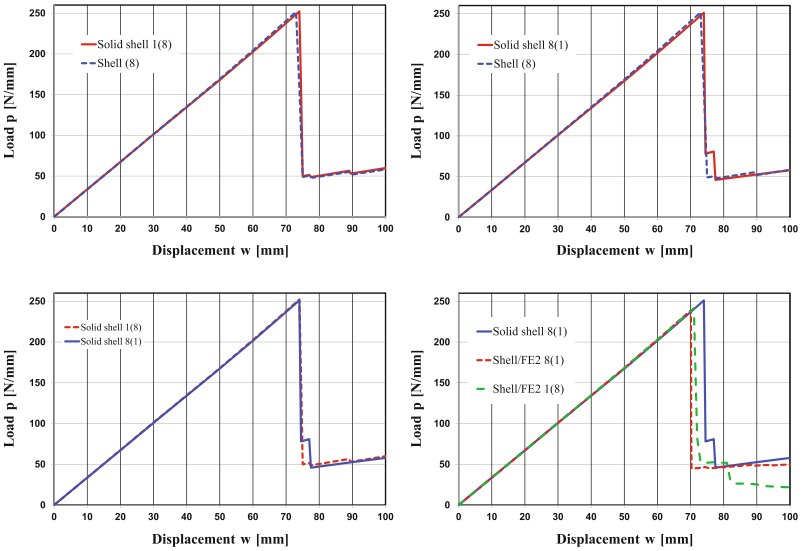

Fig. 5 Hashin-Failure model. Load-deflection curves for different discretisation models

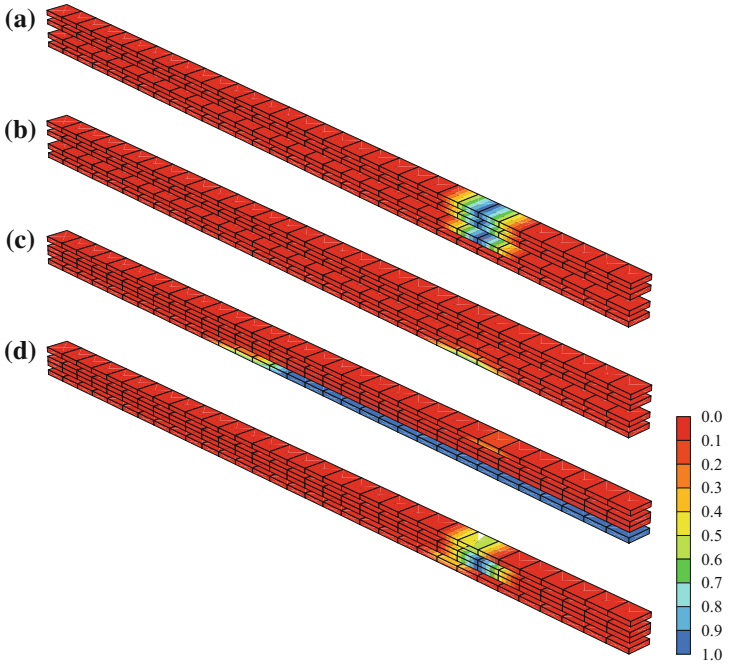

Fig. 6 Hashin-Failure model in Solid Shell at w = 100 mm **a** $FF(0°)$, **b** $M^t(0°)$, **c** $M^t(90°)$, **d** $M^c(90°)$

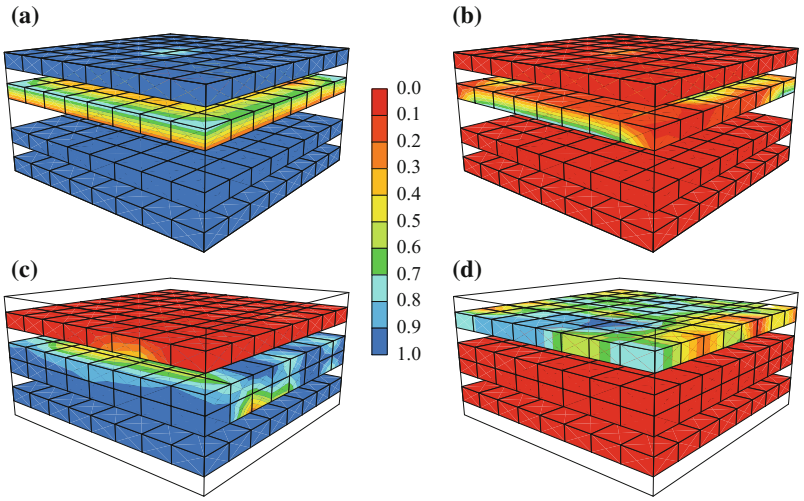

Fig. 7 Hashin-Failure model in Shell-FE2 at w = 100 mm **a** $FF(0°)$, **b** $FMS(0°)$, **c** $M^t(90°)$, **d** $M^c(90°)$

element 24, Gauss-point 1, which is near the loading area. As can be seen from Fig. 7, the failure behaviour in the 'Shell-FE2 8(1)' model, is dominated by failure $FF(0°)$ at top (c) and bottom (t), $FMS(0°)$ and $M^t(90°)$, $M^c(90°)$.

4.3 Puck-Model

Again load-deflection curves for different discretisation models, now in case of the Puck failure model, are depicted in Fig. 8. As can be seen from the diagram similar results are produced for a discretisation 'Solid Shell 1(8) and a standard shell formulation 'Shell (8)'. These results deviate from the model 'Solid Shell 8(1)', where a more complex post-failure region occurs. The multi-scale solutions 'Shell FE2 1(8)' and 'Shell FE2 8(1)' have lower failure loads than 'Solid Shell 8(1)' but a similar post-critical behaviour. The distribution of damaged areas can be seen again in Figs. 9 and 10. The detailed failure behaviour is similar to the Hashin-model. Failure modes occur for $FF(0°)$ at top (c) and bottom (t), $IFF\,B(0°)$ and $IFF\,A = M^t(90°)$, $IFF\,C = M^c(90°)$.

4.4 Cuntze-Model

The Cuntze-model is based on similar concepts as the Puck-model. Thus it could be expected, that the load-deflection behaviour for this model lies in the same range, see Fig. 11. Again similar results are produced for discretisation 'Solid Shell 1(8)' and 'Shell (8)'. Also these results do not show the more complex post failure behaviour, which occur for model 'Solid Shell 8(1)'. The multi-scale solutions 'Shell

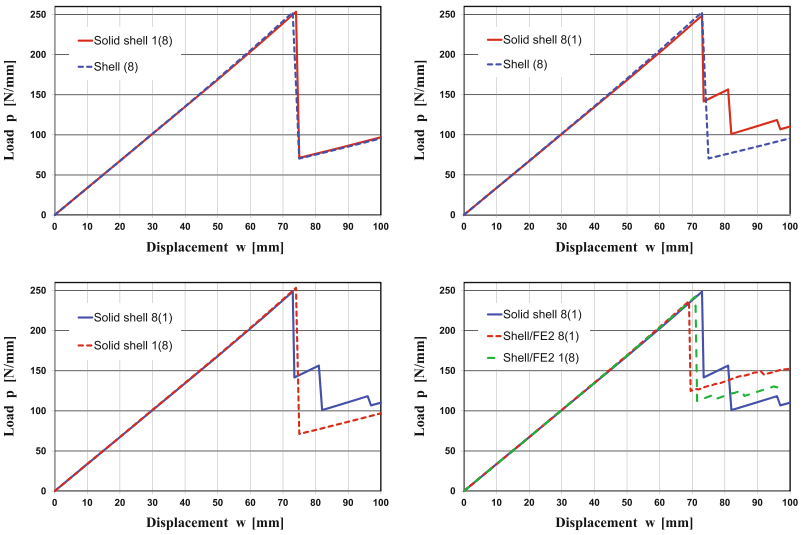

Fig. 8 Puck-Failure model. Load-deflection curves for different discretisation models

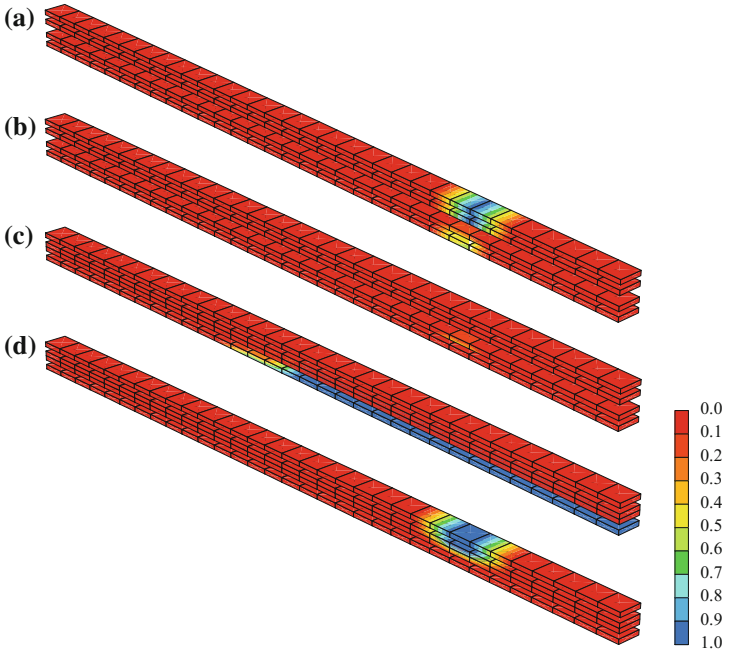

Fig. 9 Puck-Failure model in Solid Shell at w = 100 mm **a** $FF(0°)$, **b** $IFF\,A(0°)$, **c** $IFF\,A = M^I(90°)$, **d** $IFF\,C = M^c(90°)$

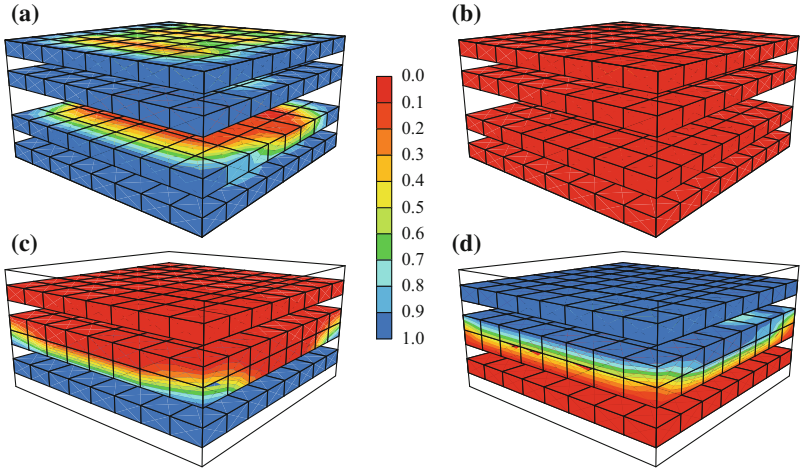

Fig. 10 Puck-Failure model in Shell-FE2 at w = 100 mm **a** $FF(0°)$, **b** $IFFB(0°)$, **c** $IFFA = M^t(90°)$, **d** $IFFC = M^c(90°)$

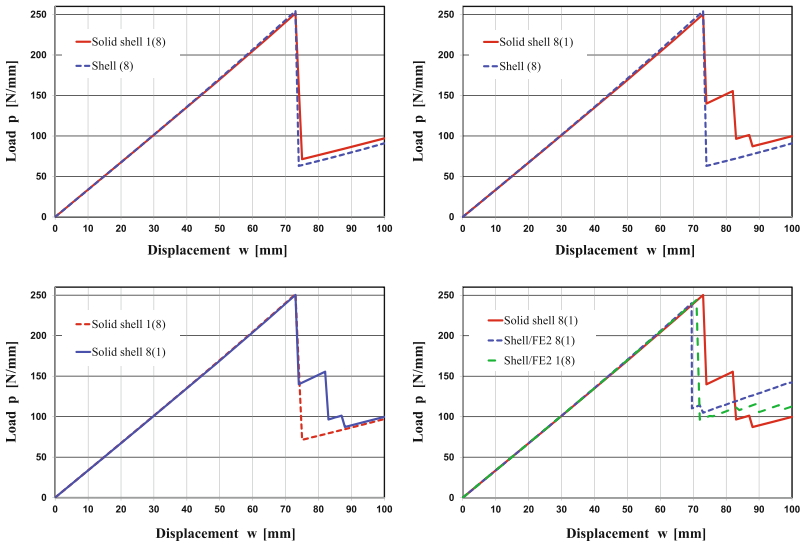

Fig. 11 Cuntze-Failure model. Load-deflection curves for different discretisation models

FE2 1(8)' and 'Shell FE2 8(1)' have lower failure loads than 'Solid Shell 8(1)' but describe the post-critical behaviour in a similar way. The distribution of damaged areas can be seen again in Figs. 12 and 13. The detailed failure behaviour for the Cuntze-model is governed by $FF(0°)$ at top (c) and bottom (t), $IFF1(0°)$ and $IFF1 = M^t(90°)$, $IFF3 = M^c(90°)$ and is close to the results of the Puck-model.

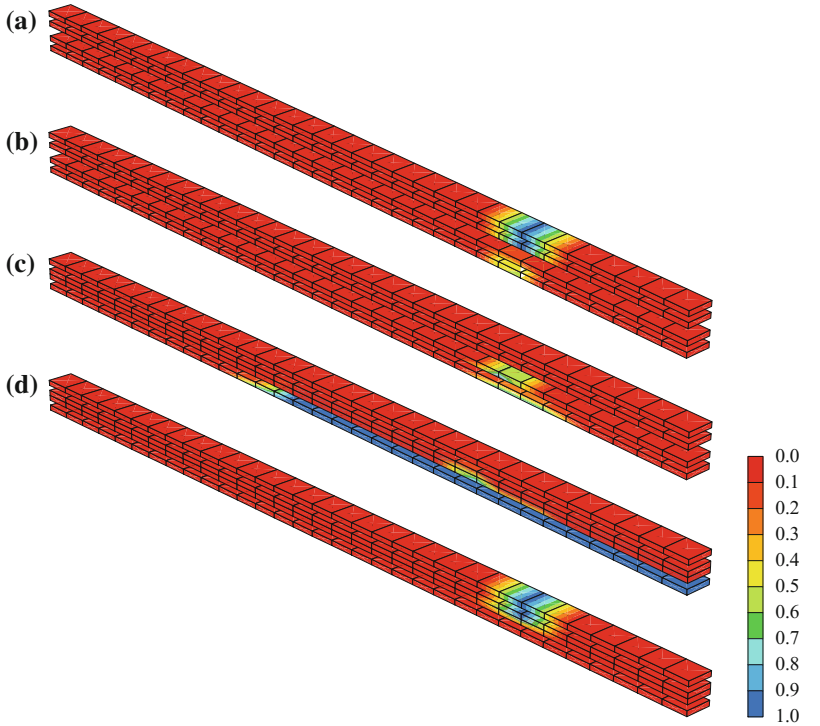

Fig. 12 Cuntze-Failure model in Solid Shell at w = 100 mm **a** $FF(0°)$, **b** $IFF1 = M^t(0°)$, **c** $IFF1 = M^t(90°)$, **d** $IFF3 = M^c(90°)$

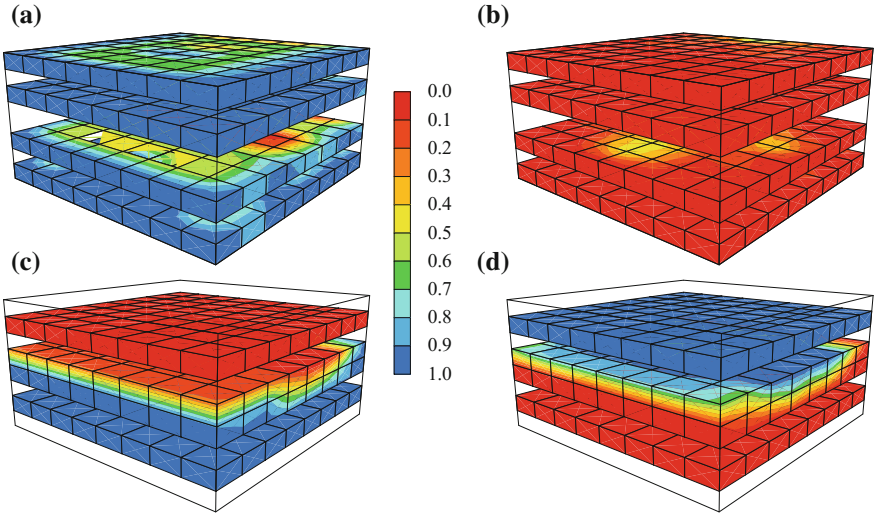

Fig. 13 Cuntze-Failure model in Shell-FE2 at w = 100 mm **a** $FF(0°)$, **b** $IFF1 = M^t(0°)$, **c** $IFF1 = M^t(90°)$, **d** $IFF3 = M^c(90°)$

5 Conclusions

Different discretisation concepts for thin shell structures with respect to damage behaviour have been discussed in this paper. These concepts are layered solid shell models, layerwise solid shell models, layerwise shell models and shell models with a FE^2-approach. Layerwise solid shell and shell models possess a similar number of unknowns. The layered solid shell models allows the studying of possible warping in thickness direction. The multi-scale models are chosen with associated RVE discretisations. Results for the pre-damage behaviour are very close together for all models. No influences of different kinematic models occur for the chosen example, see Figs. 5, 8 and 11. Damage behaviour is described via three different failure models. Obviously these models lead to different estimations for the post-failure behaviour. Nevertheless the general failure behaviour could be described with all models, when matrix-failure in the 90°-layer at bottom, fiber failure in the 0°-layer at top and another matrix-failure in the 90°-layer at top occur. However, in detail, different load deflection curves are predicted in the post-failure region. The influence of the failure models are presented in Fig. 14. Results using layerwise solid shell elements for the Puck- and Cuntze-model are comparable, whereas the Hashin-model leads to a more conservative interpretation in the post-failure region. This is also reflected when choosing the shell-FE^2 approach. With respect to Figs. 7, 10 and 13 it could be stated that the shell-FE^2-approach gives much more insight into the local behaviour at integration points. Finally it should be stated that such detailed results could be reached only after time-consuming calculations. Improvements are adaptive schemes, see e.g. [22] as well as parallelisation techniques, see e.g. [13], for which multi-scale models are well suited ([2, 6]).

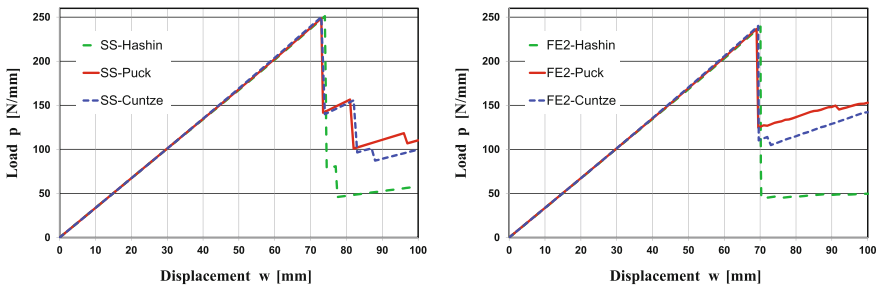

Fig. 14 Load-deflection curves for different discretisation and failure models

References

1. Carrera, E.: Historical review of zig-zag theories for multilayered plates and shells. Appl. Mech. Rev. **56**, 237–308 (2003)
2. Coenen, E., Kouznetsova, V., Geers, M.: Computational homogenization for heterogeneous thin sheets. Int. J. Num. Method Eng. **83**, 1180–1205 (2010)
3. Cuntze, R.G., Freund, A.: The predictive capability of failure mode concept-based strength criteria for multi-directional laminates. Compos. Sci. Technol. **64**, 343–377 (2004)
4. Cuntze, R.G.: The predictive capability of failure mode concept-based strength criteria for multi-directional laminates—part b. Compos. Sci. Technol. **64**, 487–516 (2004)
5. De Borst, R., Ramm, E.: Multiscale methods in computational mechanics: progress and accomplishments. In: Springer Series: Lecture Notes in Applied and Computational Mechanics, vol. 55. Springer, Berlin, Heidelberg (2011)
6. Geers, M., Coenen, E., Kouznetsova, V.: Multi-scale computational homogenization of structured thin sheets. Model. Simul. Mater. Sci. Eng. **15**, 393–404 (2007)
7. Goyal, V.K., Jaunky, N., Johnson, E.R., Ambur, D.R.: Intralaminar and interlaminar progressive failure analyses of composite panels with circular cutouts. Compos. Sci. Technol. **64**, 91–105 (2004)
8. Gruttmann, F., Wagner, W.: Coupling of 2D- and 3D-composite shell elements in linear and nonlinear applications. Comp. Meth. Appl. Mech. Eng. **129**, 271–287 (1996)
9. Gruttmann, F., Wagner, W.: Structural analysis of composite laminates using a mixed hybrid shell element. Comput. Mech. **37**, 479–497 (2006)
10. Gruttmann, F., Wagner, W.: A coupled two-scale shell model with applications to layered structures. Int. J. Num. Method Eng. **94**, 1233–1254 (2013)
11. Gruttmann, F., Wagner, W., Knust, G.: A coupled global-local shell model with continuous interlaminar shear stresses. Comput. Mech. **57**, 237255 (2016)
12. Hashin, Z.: Failure criteria for unidirectional fiber composites. J. Appl. Mech. **47**, 329–334 (1980)
13. Jarzebski, P., Wisniewski, K., Taylor, R.L.: On parallelization of the loop over elements in FEAP. Comput. Mech. **56**, 77–86 (2015)
14. Klinkel, S., Gruttmann, F., Wagner, W.: A continuum based 3d-shell element for laminated structures. Comput. Struct. **71**, 43–62 (1999)
15. Klinkel, S., Gruttmann, F., Wagner, W.: A robust non-linear solid shell element based on a mixed variational formulation. Comp. Meth. Appl. Mech. Eng. **195**, 179–201 (2006)
16. Puck, A., Schürmann, H.: Failure analysis of FRP laminates by means of physically based phenomenological models. Compos. Sci. Technol. **58**, 1045–1067 (1998)
17. Puck, A., Kopp, J., Knops, M.: Guidelines for the determination of the parameters in Pucks action plane strength criterion. Compos. Sci. Technol. **62**, 371378 (2002)
18. Reddy, J.N.: Mechanics of Laminated Composite Plates and Shells: Theory and Analysis. CRC Press, London (2004)
19. Taylor, R.: FEAP. http://www.ce.berkeley.edu/projects/feap/
20. Wagner, W., Gruttmann, F.: A robust nonlinear mixed hybrid quadrilateral shell element. Int. J. Num. Meth. Eng. **64**, 635–666 (2005)
21. Wagner, W., Gruttmann, F.: A consistently linearized multi-scale model for shell structures. In: Pietraszkiewicz, W., Górski, J. (eds.) Shell Structures: Theory and Applications, vol(3), pp. 453–456. Taylor & Francis, London (2013)
22. Wagner, W., Gruttmann, F.: An adaptive strategy for the multi-scale analysis of plate and shell structures with elasto-plastic material behaviour. Technische Mechanik **36**(1–2), 132–144 (2016)
23. Zohdi, T., Wriggers, P.: Introduction to Computational Micromechanics. Springer Series: Lecture Notes in Applied and Computational Mechanics, vol. 20. Springer, Berlin, Heidelberg (2005)